Highly Charged Cations from *N*,*N*,*N*′,*N*′-Tetrakis(4-aminophenyl)benzidine and Its *N*,*N*,*N*′,*N*′-Tetrakis(4-methoxyphenyl)-Substituted Homologue Studied by Thin-Layer in Situ Electron Spin Resonance/UV−Vis−NIR Spectroelectrochemistry

Martin Matis,[†,‡] Peter Rapta,[†,‡] Vladimír Lukeš,[†,‡] Horst Hartmann,[§] and Lothar Dunsch*[,†]

Center of Spectroelectrochemistry, Department of Electrochemistry and Conducting Polymers, IFW Dresden, Helmholtzstrasse 20, D-01069 Dresden, Germany, Faculty of Chemical and Food Technology, Department of Physical Chemistry, Slovak University of Technology, Radlinského 9, SK-812 37 Bratislava, Slovak Republic, and Institute of Applied Photophysics, University of Technology, George-Bähr-Strasse 1, D-01069 Dresden, Germany

Received: December 28, 2009; Revised Manuscript Received: February 22, 2010

The redox behavior of *N*,*N*,*N*′,*N*′-tetrakis(4-aminophenyl)benzidine (**A**) and its *N*,*N*,*N*′,*N*′-tetrakis(4-methoxyphenyl)-substituted analogue (**B**) was studied in detail by a new designed in situ thin layer electron spin resonance (ESR)/UV−vis−NIR spectroelectrohemical cell. The spectroelectrochemical studies of cation radicals, dications, and tetracations indicate a strong difference in stability of higher ions of two model compounds with different phenyl substitution. In cyclovoltammetry the small peak separation of the first two oxidation peaks for both compounds points to a small energetic difference in the first two electron transfers, while the peak separation of the second and third peak is quite large. A well resolved ESR spectrum of the $\mathbf{B}^{\bullet+}$ cation radical with dominating splittings from two nitrogen atoms is observed and an ESR silent product was determined at the third oxidation peak for both compounds, confirming the formation of a tetracation by a two electron transfer at the third voltammetric peak. In contrast to structure **A** a more complex redox behavior was found for **B** under voltammetric cycling. The reaction mechanism indicates the transformation of **B** in a new product **P** with a carbazole moiety. This compound can form a highly stabilized cation radical $\mathbf{P}^{\bullet+}$. A theoretical study based on density functional theory calculations has clarified the role of charging in changes to the structures of both triarylamine derivatives **A** and **B**.

Introduction

Recently, aromatic or heteroaromatic compounds of high redox activity in reversible processes have received a lot of interest. Especially *N*-perarylated aromatic amines, diamines, and triamines can be used as materials in opto-electronic devices, such as organic photocopiers, OLEDs, OSOLs, and solar cells because of the reversibility of the appropriate electron transfer processes.[1−6] The combined application of electron spin resonance (ESR) and UV−vis−NIR spectroscopy as well as cyclic voltammetry (CV) gives rise to detailed information of redox processes by elucidating the chemical structure and the electronic nature of the reduced or oxidized species generated in multistep electron transfer processes.[7−10]

The electrochemical oxidation of molecules to higher cations leads to the formation of differently charged compounds that can undergo symproportionation/disproportionation reactions in the bulk solution giving rise to products with different charges and spins. Consequently, the experimental (e.g., UV−vis−NIR) spectra can be superimposed in solution by absorptions of different species. Here symproportionation/disproportionation reactions of molecules with open-shell structure can be generated or annihilated. To overcome these difficulties of the formation of several charged states at a distinct electrode potential spectroelectrochemical measurements in thin-layer cells (TLC) are recommended.[11−14] On the other hand if high quality ESR spectra of ion radicals are of interest, a symproportionation reaction of doubly charged and initial neutral molecule in the bulk solution to form two paramagnetic ion radicals ($\mathbf{A} + \mathbf{A}^{2+} \rightleftharpoons 2\mathbf{A}^{\bullet+}$) is very helpful. Thus even in two-electron transfers it is possible to monitor the ESR spectra of ion radicals as already illustrated for conducting oligomers and polymers as well as fullerene dimers.[15−17] Therefore, both experimental approaches including special thin layer cells as well as spectroelectrochemistry in electrochemical ESR flat cells are of high interest for detailed studies in multistep processes of organic redox systems.

Organic electrochromics are mainly based on reversible two-step processes in redox systems that display distinct changes of their absorption spectra in different oxidation states. Recently, the two-electron redox process in violene-typed molecules for electrochromic application was detected and analyzed where both electrochemical steps have a small energetic gap.[18] A similar behavior was found in the oxidation of triarylamine derivatives and starburst compounds[19] used as materials in photocopiers or OLEDs. For these compounds the concentrations of radical cations are significantly small and the solutions dominated by dicationic and/or higher charged species. Highly charged cations have been detected in the electrochemical oxidation of α,ω-bis(diphenylamino)-substituted oligothiophenes. These compounds can be considered as heterocyclic analogues of 4,4′-bis(diphenylamino)-substituted oligophenylenes forming deeply colored dicationic species which were studied in some special structures.[20]

Although poly(aryl)amines have been the subject of numerous experimental and computational studies [see, e.g., refs 21−25]

* Corresponding author. E-mail: l.dunsch@ifw-dresden.de.
† IFW Dresden.
‡ Slovak University of Technology.
§ Technical University.

10.1021/jp912213v
Published on Web 03/12/2010

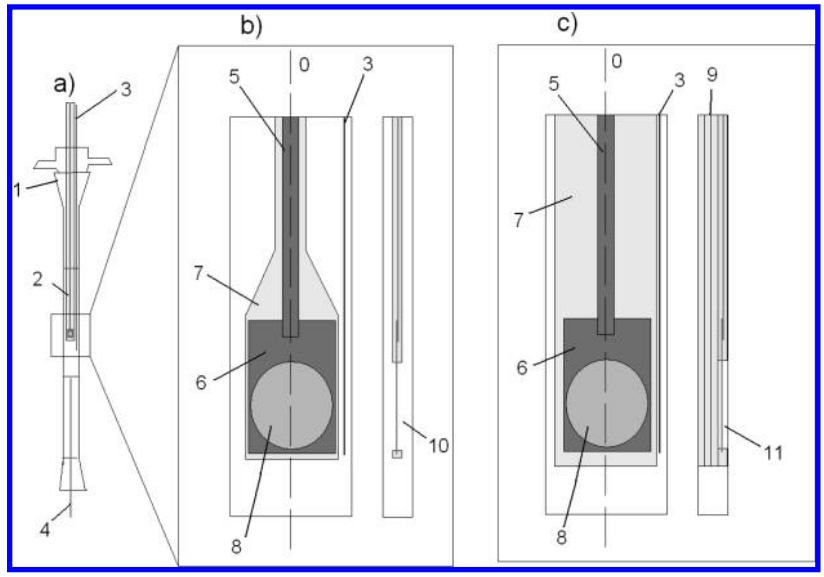

Figure 1. Scheme of (a) spectroelectrochemical cell, (b) detail of the central part of standard spectroelectrochemical cell (front and profile view), and (c) detail of the central part of thin layer spectroelectrochemical cell (front and profile view): (1, quartz ESR flat cell; 2, laminated working electrode; 3, Ag wire; 4, Pt-wire counter electrode; 5, gold foil; 6, gold-μ-mesh; 7, laminating foil; 8, electroactive surface, not laminated; 9, inert and optically transparent foil sheets; 10, electrolyte volume in standard ESR-spectroelectrochemical cell; 11, electrolyte volume in a thin layer cell).

relatively little is known about their higher charged states (more than two charges). As ESR spectroscopy gives detailed structural information on paramagnetic species and the UV−vis−NIR spectra contain information of both diamagnetic and paramagnetic species formed in complex redox reactions, we focused our attention to the properties of cation radicals, dications, and tetracations of two model compounds, *N*,*N*,*N*′,*N*′-tetrakis(4-aminophenyl)benzidine (**A**) and its *N*,*N*,*N*′,*N*′-tetrakis(4-methoxyphenyl)-substituted analogue (**B**), using cyclic voltammetry and in situ ESR/UV−vis−NIR spectroelectrochemistry. To interpret the experimental results of the in situ spectroelectrochemistry, geometry optimization of both neutral and the charged structures was performed. The electronic ground state optimal geometries for neutral and charged states (1+, 2+, 3+ and 4+) of **A** and **B** molecules were also studied theoretically using density functional theory (DFT). On the basis of optimal geometries, the vertical electronic excitation energies were calculated using the time-dependent version of DFT (TD-B3LYP).

Experimental Section

All cyclovoltammetric (CV) experiments were performed at room temperature in a glovebox (oxygen and water content below 1 ppm) using a HEKA potentiostat PG 285 with software package PotPulse 8.53 (HEKA Electronic, Germany). A standard three-electrode arrangement with a platinum wire as a working electrode, a platinum wire as a counter electrode, and a silver wire as a pseudoreference electrode was used. Ferrocene (Fc) was added as the internal standard for a final voltammetric cycle and all potentials are referred to Fc/Fc^+ couple.

In the spectroelectrochemical experiment the ESR spectra were recorded by the EMX X-Band ESR spectrometer (Bruker, Germany) and the optical spectra by the UV−vis−NIR spectrometer system TIDAS (J&M, Aalen, Germany). Both the ESR spectrometer and the UV−vis−NIR spectrometer were triggered by a HEKA potentiostat PG 285. Here, a three-electrode arrangement with a laminated working electrode with a gold-μ-mesh, a platinum wire as a counter electrode, and a silver wire as a pseudoreference electrode was used. To reach the thin layer conditions, the electrolyte volume was reduced by inert foil sheets inserted into the flat cell (see Figure 1).

N,*N*,*N*′,*N*′-Tetrakis(4-aminophenyl)benzidine **A**, purchased from Sigma Aldrich, and *N*,*N*,*N*′,*N*′-tetrakis(4-methoxyphenyl)-benzidine **B**, purchased from Sensient Imaging Technologies, Wolfen, were used as received. As supporting electrolyte $TBABF_4$ (Sigma Aldrich) was used after being dried under reduced pressure at 340 K for 24 h and stored in a glovebox prior to use. The concentration of $TBABF_4$ in dichloromethane ranges from 0.1 to 0.2 mol L^{-1}. The dichloromethane was stored in glovebox as well. The concentration of the samples ranges from 5×10^{-4} to 1×10^{-3}.

Computational Details

The electronic ground state optimal geometries for neutral and charged states (1+, 2+, 3+, and 4+) of **A** and **B** molecules were obtained using DFT.[26] The DFT calculations were performed using the B3LYP functional,[27] where Becke's three-parameter hybrid exchange functional is combined with the Lee−Yang−Parr correlation functional. On the basis of optimal geometries, the vertical electronic excitation energies were calculated using TD-B3LYP.[28] The polarized split-valence SV(P) basis set[29] was used. All calculations were done with the Gaussian 98 quantum chemical package.[30]

Results and Discussion

Electrochemical and Spectroelectrochemical Studies. The compounds under study with the numbering of selected chemical bonds are shown in Scheme 1. Cyclic voltammograms of *N*,*N*,*N*′,*N*′-tetrakis(4-aminophenyl)benzidine (**A**) in electrochemical cell in acetonitrile or in dichloromethane (scan rate 0.1 V s^{-1}) show two pairs of reversible cathodic and anodic peaks with a relatively small difference of formal redox potentials (0.00 and 0.12 V vs Fc/Fc^+) and a third peak pair at the formal potential of 0.41 V vs Fc/Fc^+ the height of which indicates a two-electron transfer (Figure 2a). The charge transferred in the first voltammetric double peak, estimated by integration of the baseline corrected current−time curve in forward scan (3.0

SCHEME 1

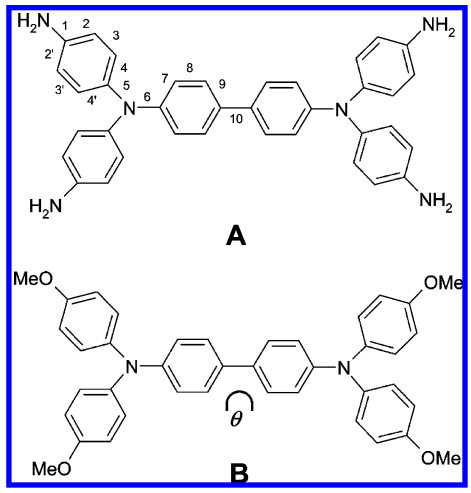

mAs), is close to the charge transferred in the third peak (2.7 mAs), confirming this assumption. On the other hand, its *N*,*N*,*N*′,*N*′-tetrakis(4-methoxyphenyl)-substituted analogue (**B**) reveals two pairs of reversible voltammetric peaks at formal redox potentials of 0.31 and 0.45 V vs Fc/Fc^+ but the third anodic peak at 1.15 V vs Fc/Fc^+ shows an irreversible behavior (Figure 2b). This is a first indication of the different stability of higher charged ions of two model compounds with different phenyl substitution.

Using in situ ESR/UV−vis−NIR spectroelectrochemistry in the spectroelectrochemical ESR flat cell at a potential scan rate of 0.004 V s^{-1} at the foot of the first anodic peak for **A** in

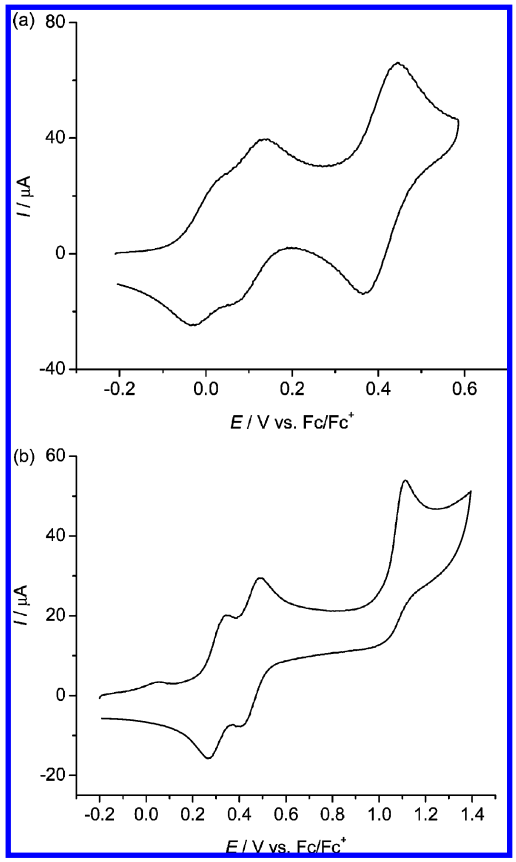

Figure 2. Cyclic voltammogram of (a) *N*,*N*,*N*′,*N*′-tetrakis(4-aminophenyl)benzidine (**A**) and its *N*,*N*,*N*′,*N*′-tetrakis(4-methoxyphenyl)-substituted homologue (**B**) in 0.2 mol dm^{-3} $TBABF_4$/dichloromethane (scan rate 0.1 V s^{-1}).

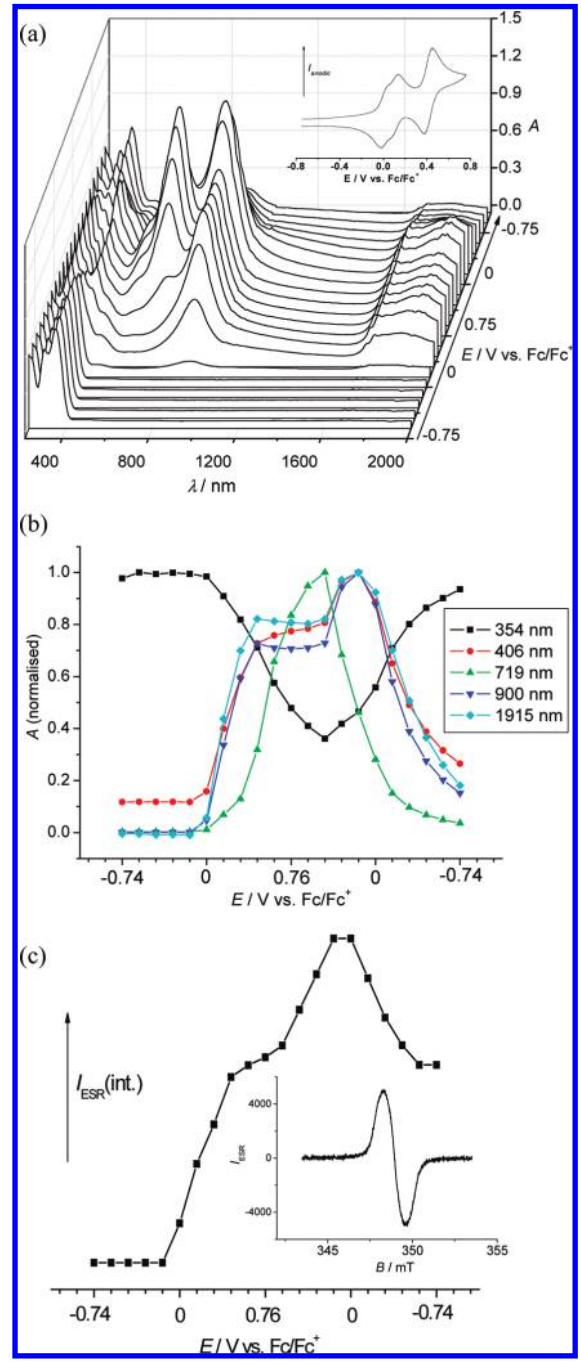

Figure 3. Spectroelectrochemistry of **A** (0.5 mM) in a standard spectroelectrochemical cell in 0.2 mol dm^{-3} $TBABF_4$/dichloromethane (scan rate 0.004 V s^{-1}): (a) potential dependence of UV−vis−NIR spectra during cyclovoltammetric scan; (b) potential dependence of the absorbances at selected wavelengths; (c) potential dependence of the integral ESR intensity.

$TBABF_4$/DCM, we observed four optical transitions at 462, 882, 1120, and 1810 nm (Figure 3). Simultaneously, broad unresolved ESR spectra at a *g*-value of 2.0027 were observed (inset in Figure 3c). The shape of ESR spectrum indicates the presence of a large set of splittings, confirming that spin density in the radical cation $\mathbf{A}^{\bullet+}$ is delocalized over a large part of the molecule. At the second electron transfer structure **A** shows a dominating absorption band at 915 nm, which is very close to the band at 882 nm of the monocation $\mathbf{A}^{\bullet+}$. This band shifts during oxidation from 882 to 915 nm. The increase of the optical bands around 900 nm at the potentials of the first voltammetric peak was connected with that of ESR intensity increasing during

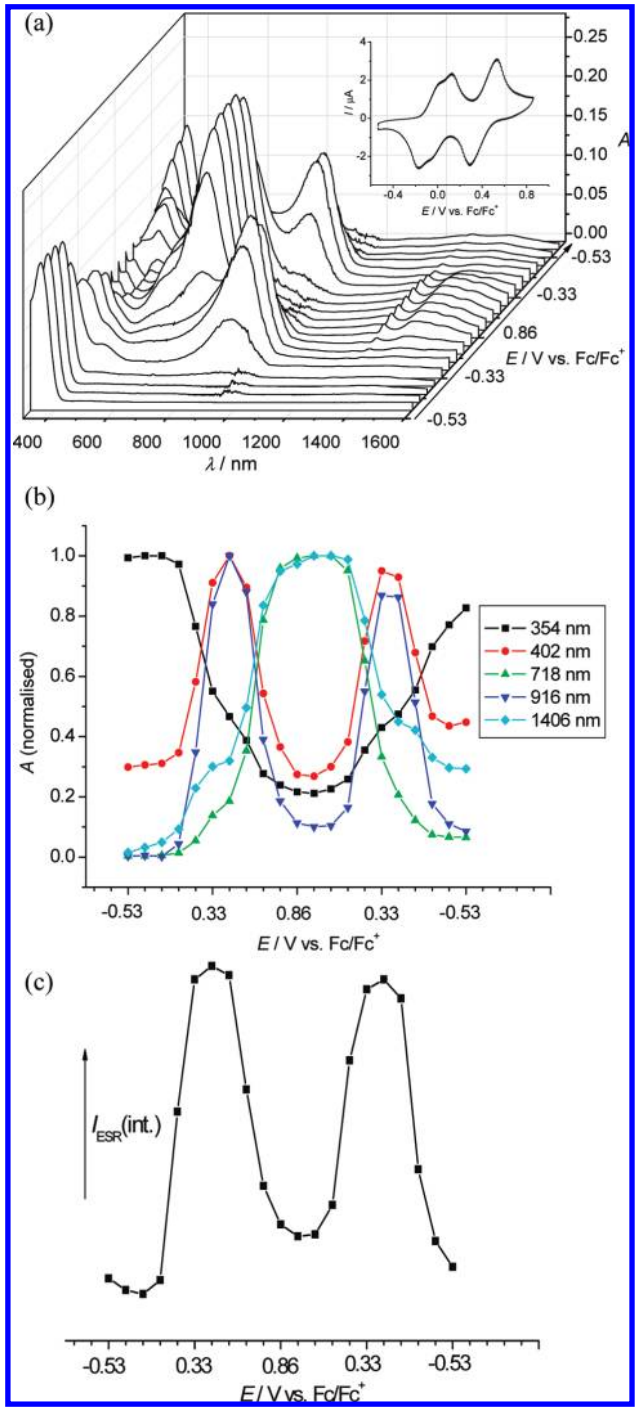

Figure 4. Spectroelectrochemistry of **A** (0.5 mM) in a thin-layer spectroelectrochemical cell in 0.2 mol dm^{-3} $TBABF_4$/dichloromethane (scan rate 0.004 V s^{-1}): (a) potential dependence of UV−vis−NIR spectra during cyclovoltammetric scan (inset: in situ cyclic voltammogram); (b) potential dependence of absorbances at selected wavelengths; (c) potential dependence of the integral ESR intensity.

the whole in situ cyclovoltammetric experiment (Figure 3c). This is due to a symproportionation reaction in the bulk solution in the spectroelectrochemical cell according to the reaction $\mathbf{A} + \mathbf{A}^{2+} \rightleftharpoons 2\mathbf{A}^{\bullet+}$. This is obvious in the potential dependence of ESR intensity of the formed cation radical in the second electron transfer, where a decrease of ESR signal is expected. We observed its increase as a concequence of symproportionation reaction in the bulk. As shown in Figure 3b this behavior also matches the potential dependencies of optical bands at selected wavelengths characteristic for $\mathbf{A}^{\bullet+}$ cation radical. At

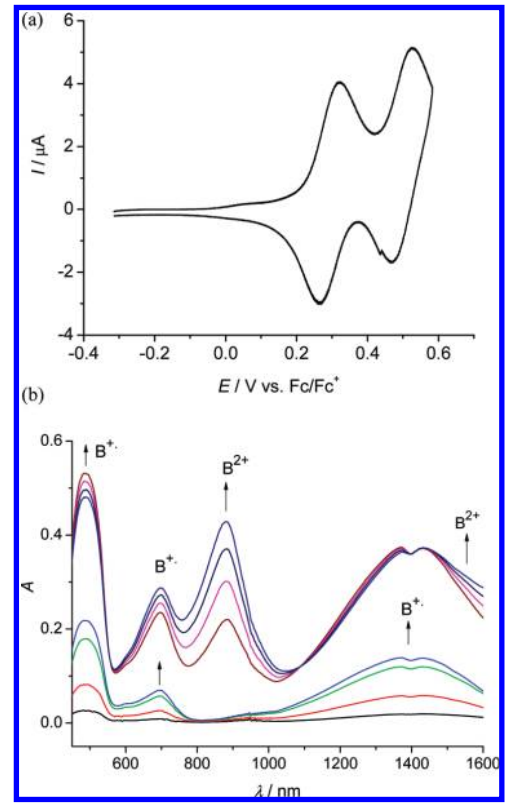

Figure 5. Spectroelectrochemistry of **B** (0.5 mM) in a standard spectroelectrochemical cell in 0.2 mol L^{-1} $TBABF_4$/dichloromethane. (a) Corresponding in situ cyclic voltammogram (scan rate 0.003 V s^{-1}) and (b) representative UV−vis−NIR spectra of cation radical $\mathbf{B}^{\bullet+}$ and dication $\mathbf{B}^{2+}$ measured during a cyclovoltammetric scan to the first and second oxidation peak, respectively.

the third oxidation peak the absorption at 915 nm decreases and a new dominating band at 720 nm arises via an isosbestic point at 795 nm. This new band can be ascribed to tetracation $\mathbf{A}^{4+}$. In addition to the dominating band at 720 nm a small new band around 1440−1600 nm also arises at the third cyclovoltammetric peak.

In a thin layer ESR/UV−vis−NIR cyclovoltammetric experiment of structure **A** the same optical bands were observed but the potential dependencies of ESR signal and the optical transitions are completely different. The ESR intensity reaches its maximum in both the forward and back scans (Figure 4). Additionally, a minimum ESR intensity was monitored at the third oxidation peak (Figure 4c). The increase of the absorbance at dominating band at 462 nm and at around 900 nm corresponds to the increase of the ESR intensity. At negligible ESR intensity at the third oxidation peak the absorption bands at 720 and 1500 nm dominate the spectrum (Figure 4b). At the potentials where the absorbances at 720 and 1500 nm show a maximum, the ESR intensity has a minimum. Therefore, the product of the oxidation of compound **A** at the third oxidation peak is proved to be diamagnetic and corresponds to the stable tetracation $\mathbf{A}^{4+}$. Only small amounts of a trication are formed, probably exhibiting a small transition at 1500 nm, as will be discussed in theoretical studies below.

ESR/UV−vis−NIR spectroelectrochemistry of the structure **B** shows spectroelectrochemical behavior quite similar to that for the first two electron transfers, as observed for structure **A** described above, but due to higher cyclovoltammetric as well as optical peak/band separation, the monocation and dication are more clearly observable (see Figure 5). A well-defined UV−vis−NIR spectrum of cation radical $\mathbf{B}^{\bullet+}$ with band maxima at 490, 880, and 1385 nm was observed, which dominates the optical spectra in the potential range at first cyclovoltammetric

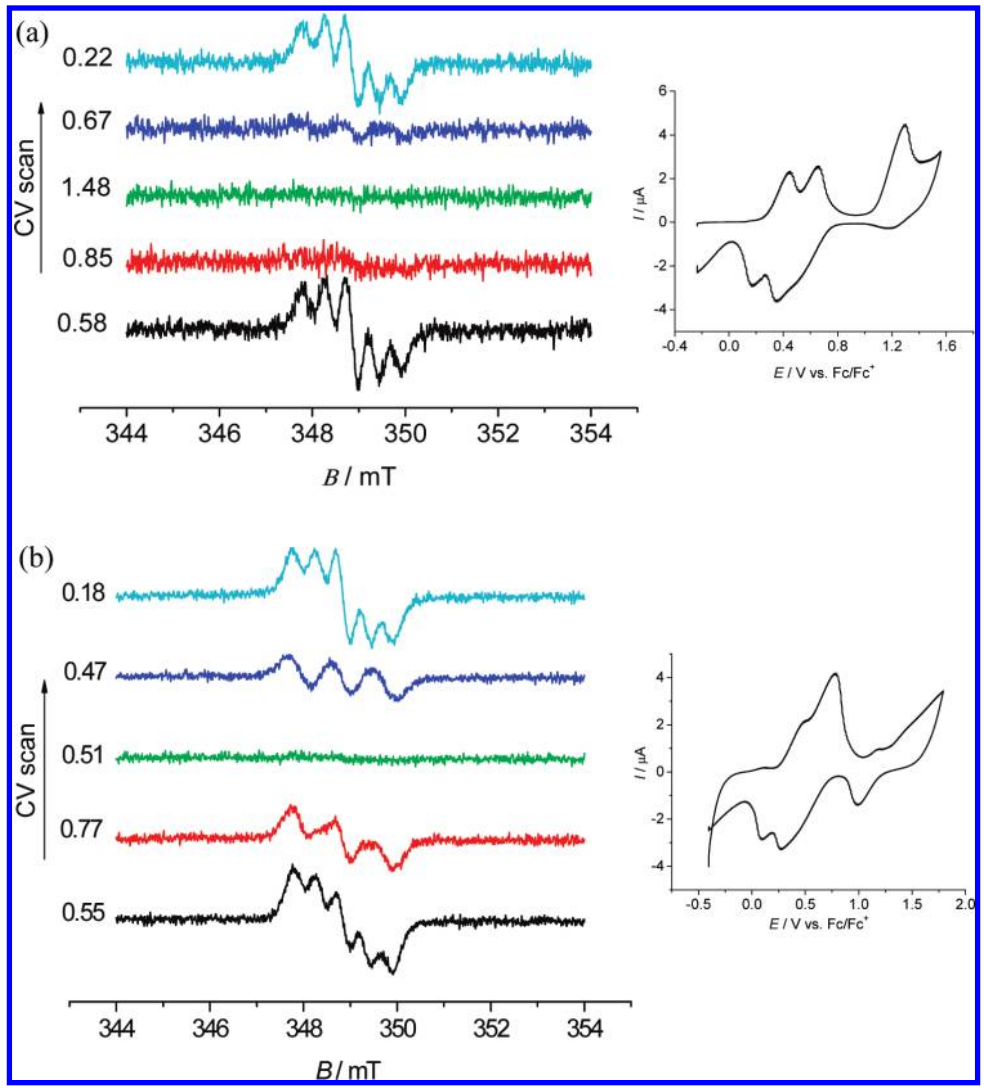

Figure 6. Selected ESR spectra at certain potentials obtained in a thin layer spectroelectrochemical measurement of compound **B** in 0.2 mol dm^{-3} $TBABF_4$/dichloromethane during (a) the first and the second cyclovoltammetric scan. Inset: in situ cyclic voltammogram (scan rate 0.004 V s^{-1}).

peak. However, a better resolved ESR spectrum of the cation radical was observed with two equivalent nitrogen splittings in contrast to compound **A**, indicating a different spin distribution in the radical cations $\mathbf{A}^{\bullet+}$ and $\mathbf{B}^{\bullet+}$. Going to the second electron transfer, structure **B** shows a dominating absorption band at 880 nm and a decrease in ESR intensity. At the third oxidation peak we found only a slight shift of the band at 880 nm to the higher energies. The absence of an ESR signal at the third oxidation peak in the first voltammetric scan indicates a two-electron transfer similar to **A**. However, the oxidation of **B** is not completely chemically reversible in this potential region. A repeated voltammetric cycling gives a new triplet-like ESR spectrum, as indicated in Figure 6. In addition, new reduction peaks arise in the back scan and a much more complex redox behavior was found under repeated cycling and thin-layer conditions. The intensity of the new ESR signal with a large spitting constant of one nitrogen ($a_N = 0.9$ mT) continuously increases during the voltammetric cycling of **B** going up to the third oxidation peak. Already in the second cyclovoltammetric scan this new ESR spectrum is observable at the new oxidation peak at around 0.45 V vs Fc/Fc^+. Simultaneously, the intensity of the third irreversible oxidation peak of the first scan dramatically decreased, which indicates a decrease in the concentration of the compound **B** near the electrode under formation of new species **P** giving rise to a new redox cascade including the monocationic $\mathbf{P}^{\bullet+}$ and dicationic species $\mathbf{P}^{2+}$. As the ESR intensity of the new oxidation product increases during the voltammetric cycling, a fairly good stability of the new cation radical $\mathbf{P}^{\bullet+}$ can be assumed. Using the data of the thin layer ESR/UV−vis−NIR spectroelectrochemistry for the compound **B** (Figure 7), the absorption at 770 nm is attributed to $\mathbf{P}^{\bullet+}$ and that of 530 nm to $\mathbf{P}^{2+}$. On the basis of literature data of a carbazole formation by arylamino compounds upon oxidation[31] and the high stability of such carbazole cation radicals,[31,32] we propose a reaction mechanism with the transformation of $\mathbf{B}^{4+}$ in a new product $\mathbf{P}^{2+}$ assuming a compound with a carbazole moiety (Scheme 2). Reducing $\mathbf{P}^{2+}$ in a voltammetric back scan forms the neutral **P**. In the second voltammetric scan this compound can form a highly stabilized cation radical $\mathbf{P}^{\bullet+}$ with dominating nitrogen splitting, as discussed (see inset in Figure 7).

Theoretical Studies. To understand the properties of charged states of both model compounds, the optimal geometries of initial neutral states were determined by the B3LYP method in first step. The presence of single bonds connecting the chromophoric groups of the molecules under study leads to the formation of a number of conformations that differ in the mutual orientations of phenylene units. With respect to this fact, our

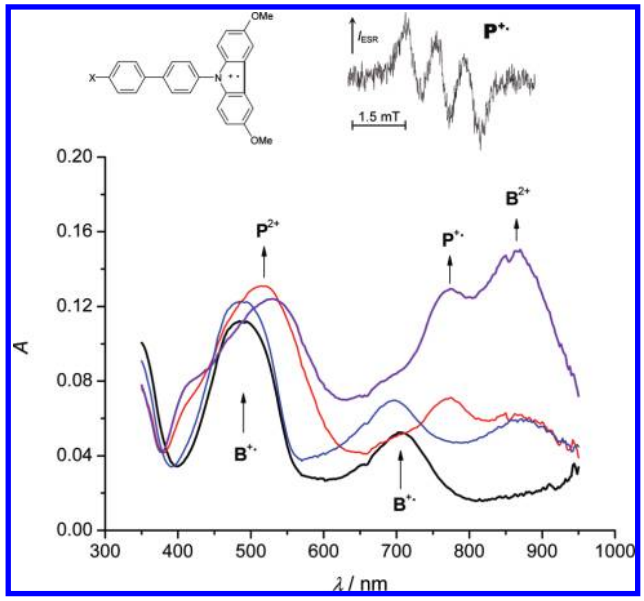

Figure 7. UV−vis−NIR spectra of cation radical $\mathbf{B}^{\bullet+}$, dication $\mathbf{B}^{2+}$, and oxididation product **P** with a carbazole moiety observed during second cyclovoltammetric in a thin layer spectroeelctrochemcial cell in 0.2 mol dm^{-3} $TBABF_4$/dichloromethane.

SCHEME 2

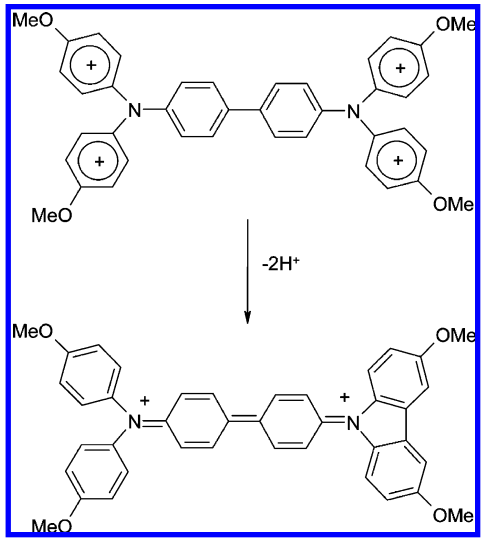

calculations started from the geometries belonging to the C_2 point symmetry; i.e., the all-trans conformation for **B** was used (see the notation and side view on the optimized **B** structure in Scheme 3). The molecules were oriented in such way that the torsional axis of biphenylene moieties coincides with the *y*-axis. The selected optimal dihedral angles of the neutral molecules in the electronic ground state are collected in Tables 1 and 2. The dihedral angle θ between the phenylene rings in **A** (**B**) molecule is twisted by 33 (34)°, which is comparable with the value of 37° obtained for the biphenyl molecule at the B3LYP/SVP level of theory.[33] Due to the identification of the symmetric conformations after the geometry optimization, only a selected number of bonds are presented in Tables 1 and 2. The largest C−C bond distances are found between the phenylene rings (see bond no. 10). The mutual changes in the lengths for the rest bonds within the phenylene units have alternating character where the difference between the neighboring bonds in absolute value is up to the 1.2 pm. This indicates the aromatic character of the central part of molecule.

SCHEME 3

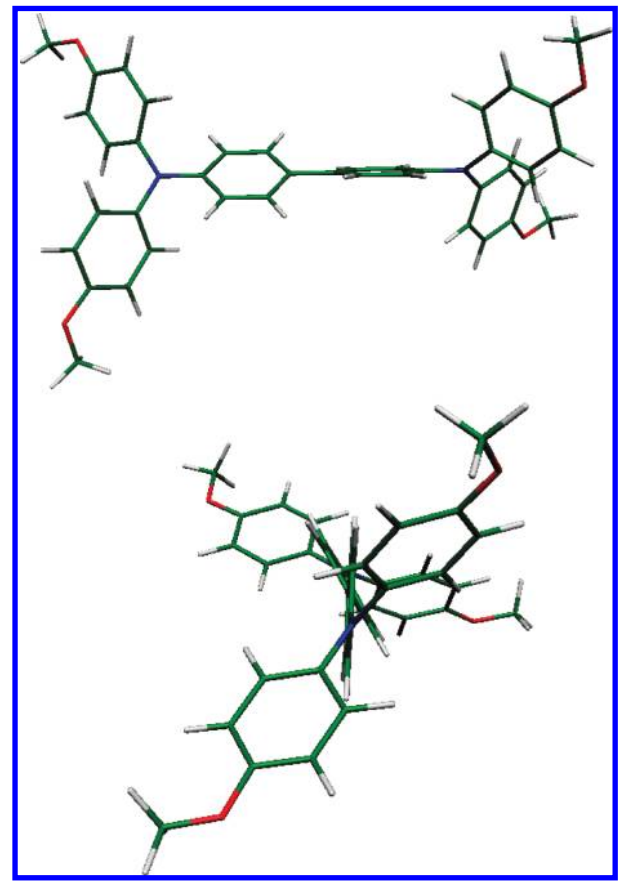

To characterize the optical transitions, it is useful to examine the occupied and the unoccupied molecular orbitals contributing to the first and lowest energy electronic transitions. The plots of the highest occupied (HOMO) and lowest unoccupied (LUMO) B3LYP orbitals dominantly contributing to the lowest excitation energy of studied systems are given in Figure 8. This transition has predominantly $\pi-\pi^*$ character and for the **A** molecule is connected mostly with the central biphenyl part where the HOMO and LUMO orbitals are delocalized. The transition for the molecule **B** is spreading from the terminal triphenylamine parts (see HOMO) into the central biphenyl part (see LUMO). The LUMOs are delocalized along the biphenyl moiety and have inter-ring bonding character. This indicates possible shortenings of the corresponding inter-ring CC distances in the lowest excited state.

The differences in the electrochemical properties of **A** and **B** molecules can be roughly estimated from the next lowest occupied orbitals, which are given in Figure 8. The HOMO−1 of molecule **A** is delocalized mostly over both terminal diphenylamine moieties. On the other hand, the HOMO−1 of molecule **B** has an energy and shape identical to that of the HOMO orbital.

To interpret the experimental results of the in situ spectroelectrochemistry, geometry optimization of the charged structures was performed in the first step. The quantum chemical calculations started from the optimized B3LYP/SV(P) neutral ground state geometries where the total electric charge and spin multiplicities of the molecule were changed. The selected dihedral angle θ and the optimal bond lengths are collected in Tables 1 and 2. The comparison of the dihedral angle θ for both molecules (see Scheme 1) reveals that the charging has a different effect on molecular planarity with respect to the extent

TABLE 1: Selected B3LYP/SV(P) Optimal Bond Lengths (in pm) and Dihedral Angle θ (in deg) of Compound A[a]

charge bond numbers	**A**	$\mathbf{A}^{\bullet+}$	$\mathbf{A}^{2+}$	$\mathbf{A}^{\bullet3+}$	$\mathbf{A}^{4+}$
1	139.3	136.9	135.4	134.2	133.0
2 (2′)	140.9 (140.9)	141.5 (141.5)	142.3 (142.3)	143.1 (143.1)	144.1 (144.1)
3 (3′)	139.4 (139.4)	138.9 (138.9)	138.3 (138.3)	137.6 (137.6)	137.0 (137.0)
4 (4′)	140.6 (140.6)	140.8 (140.8)	141.5 (141.5)	142.4 (142.4)	143.3 (143.3)
5	142.4	142.2	141.3	139.8	138.5
6	141.0	139.6	139.2	141.8	143.9
7	141.0	141.7	142.0	141.1	140.7
8	139.3	138.5	138.1	138.8	139.3
9	140.9	141.7	142.4	141.7	141.3
10	148.2	146.6	145.6	147.6	149.0
dihedral angle	**A**	$\mathbf{A}^{\bullet+}$	$\mathbf{A}^{2+}$	$\mathbf{A}^{\bullet3+}$	$\mathbf{A}^{4+}$
θ	33	25	17	27	32

[a] For the bond numbering see Scheme 1.

TABLE 2: Selected B3LYP/SV(P) Optimal Bond Lengths (in pm) and Dihedral Angle θ (in deg) of Compound B[a]

charge bond numbers	**B**	$\mathbf{B}^{\bullet+}$	$\mathbf{B}^{2+}$	$\mathbf{B}^{\bullet3+}$	$\mathbf{B}^{4+}$
1	136.0	134.5	132.9	131.2	129.6
2 (2′)	140.3 (140.7)	140.7 (141.1)	141.4 (141.8)	142.5 (142.6)	143.5 (143.4)
3 (3′)	140.0 (139.0)	139.6 (138.6)	139.0 (138.1)	138.3 (137.5)	137.5 (136.9)
4 (4′)	140.2 (141.0)	140.3 (141.0)	141.0 (141.6)	142.1 (142.6)	143.2 (143.5)
5	142.2	142.6	141.8	140.0	138.7
6	141.3	139.1	138.4	141.5	143.5
7	140.9	141.9	142.4	141.3	140.9
8	139.3	138.3	137.8	138.8	139.2
9	140.9	142.0	142.8	141.8	141.4
10	148.4	146.6	145.0	147.6	149.0
dihedral angle	**B**	$\mathbf{B}^{\bullet+}$	$\mathbf{B}^{2+}$	$\mathbf{B}^{\bullet3+}$	$\mathbf{B}^{4+}$
θ	34	13	15	25	31

[a] For the bond numbering see Scheme 1.

of oxidation. The significant planarity increase of the central biphenylene moiety is shown for the cationic and bicationic structures. The values of the angles are changed by about 5−8° and the preferred planarization is observed for the cationic and bicationic states of structure **B**. If the total positive charge is increased, the planarity is disturbed. For example, the dihedral angle for neutral **A** (**B**) and tetracationic state $\mathbf{A}^{4+}$ ($\mathbf{B}^{4+}$) are comparable.

The bond distances in Tables 1 and 2 for both molecules show consecutive geometrical changes in the whole molecular skeleton after charging. For example, the electron extraction leads to the formation of partially quinoid-type structures in the diphenylene moiety. The bonds are elongated or shortened in alternating sequence in intervals of 2−5 pm. The highest effect on the bond length change is observed for the terminal C-bond in molecule **A**. The value of 139.3 pm is changed to 136.9 pm (see Table 1). The geometrical changes after oxidation are also reflected in the ionization potential (IP), which can be characterized using the vertical (VIP) and adiabatic (AIP) ionization potentials. The VIP is the energy difference between the cationic and the neutral states based on the optimized geometry for the neutral states. Contrary to the VIP quantity, the AIP is calculated from the total energy belonging to the relaxed cationic geometry. The calculated VIP for molecule **A** is 5.03 eV, which is by 0.54 eV lower than the VIP for molecule **B** (5.57 eV). The adiabatic values of IP are by 0.14 eV higher (for **A** molecule is 5.17 eV and for **B** molecule is 5.46 eV). According to these results, radical cation $\mathbf{A}^{\bullet+}$ seems to have a more quinoid structure. The agreement of the theoretical IP values for molecule **A** with the experimental value 5.38 ± 0.15 eV[34] for the chemically similar 4,4′-bis(*m*-tolyphenylamino)biphenyl molecule shows that the B3LYP/SV(P) approach used may offer reliable energetic results for this type of molecules.

The higher charged states of molecules **A** and **B** have a mostly monotonous change of the bond distances, as reported for the cation radicals. Only the central molecular bond no. 10 is shortened up to the 2+ oxidation step and elongates afterward. For the $\mathbf{A}^{4+}$ structure, this bond is larger than in the neutral state. The comparison of the VIP and AIP energies for the higher ionized states offers an insight in the geometry relaxations. The data in Table 3 show a monotonic increase of differences mentioned with an increase of the total charge. Minimum differences are found for tetracationic states of the **B** molecule.

Comparison of Spectroelectrochemical and Theoretical Results. Experimental absorption spectra of the neutral molecules **A** and **B** in acetonitrile as well as in dichloromethane are dominated by two bands in the region from 250 to 450 nm. Although the chemical structures differ by the phenyl substitution, the optical spectra in the neutral state are very similar. The main absorption maxima at 355 nm (3.49 eV) are similar for both compounds (Figures 9 and 10). The second transition at higher energies is visible as a shoulder at 302 nm (4.11 eV) for **A** and at 307 nm (4.04 eV) for **B**.

The vertical excitation energies calculated at the TD-B3LYP/SV(P) level based on the corresponding optimized geometries indicate dominant oscillator strength for the first optical transition $S_0 \rightarrow S_1$, which belongs to 1^1B symmetry. For the molecule **A**, the energy is 3.24 eV with the oscillator strength $f = 1.228$. The transition energy for the molecule **B** is slightly blue-shifted to 3.29 eV with an oscillator strength $f = 1.1615$. In comparison to experimental values measured in DCM or ACN solution, these values are about 0.4 eV lower. A better agreement of

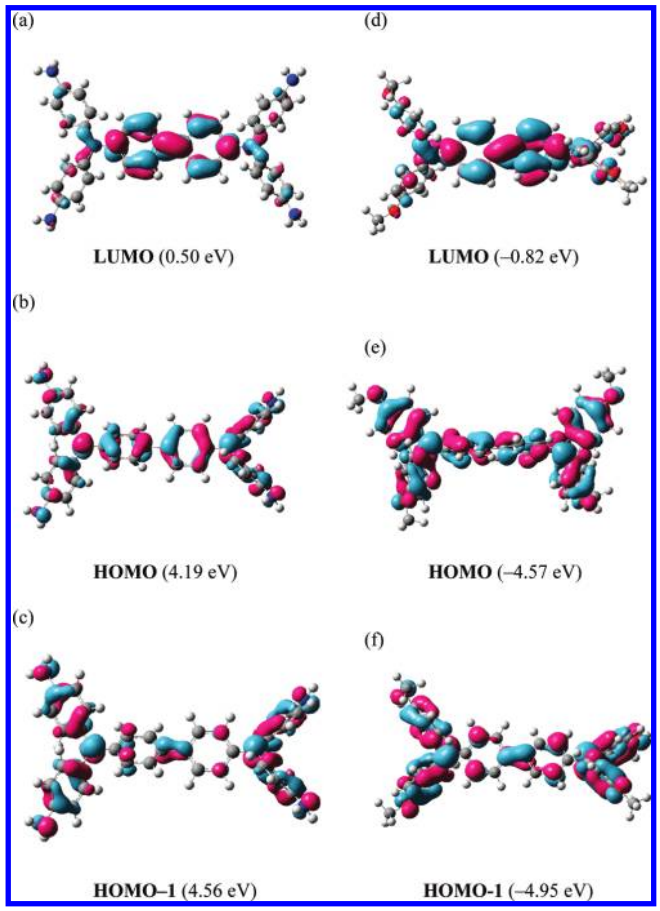

Figure 8. Selected frontier B3LYP/SV(P) orbitals for compounds **A** and **B** in their neutral state.

TABLE 3: Calculated Vertical (VIP) and Adiabatic (AIP) Ionization Potentials (in eV) for the Different Cationic States of Molecules A and B

	$\mathbf{A}^{\bullet+}$	$\mathbf{A}^{2+}$	$\mathbf{A}^{\bullet 3+}$	$\mathbf{A}^{4+}$
VIP	5.17	13.14	23.56	36.68
AIP	5.03	12.61	22.56	35.02
	$\mathbf{B}^{\bullet+}$	$\mathbf{B}^{2+}$	$\mathbf{B}^{\bullet 3+}$	$\mathbf{B}^{4+}$
VIP	5.54	13.94	24.76	38.28
AIP	5.46	13.58	24.14	37.10

experimental and theoretical results was obtained for B3LYP geometries using the semiempirical ZINDO method.[35] The standard ZINDO parametrization was performed for spectroscopic properties of π-conjugated solvated systems in their neutral states. Therefore, this method gives a better fit of experimental data and practically identical values of 3.57 eV for **A** and 3.62 eV for **B**. Despite the fact that the TD-DFT method underestimates excitation energies for the long chainlike organic systems in comparison to the semiempirical ZINDO method, its results for charged states might be more realistic. The inclusion of the solvent effect using the continuum model[36] in TD-DFT could improve the agreement with the experimental values, but the general trends obtained for the gas phase will be the same. The next nearest TD-B3LYP optical transitions with dominant oscillator strengths for molecule **A** have 6^1A symmetry (3.91 eV, $f = 0.2557$) and 9^1A symmetry (4.08 eV, $f = 0.1237$). For the molecule **B**, the next nearest optical transitions have 3^1B symmetry (3.91 eV, $f = 0.1174$), 3^1A symmetry (3.92 eV, $f = 0.1297$), and 5^1B symmetry (4.02 eV, $f = 0.1252$).

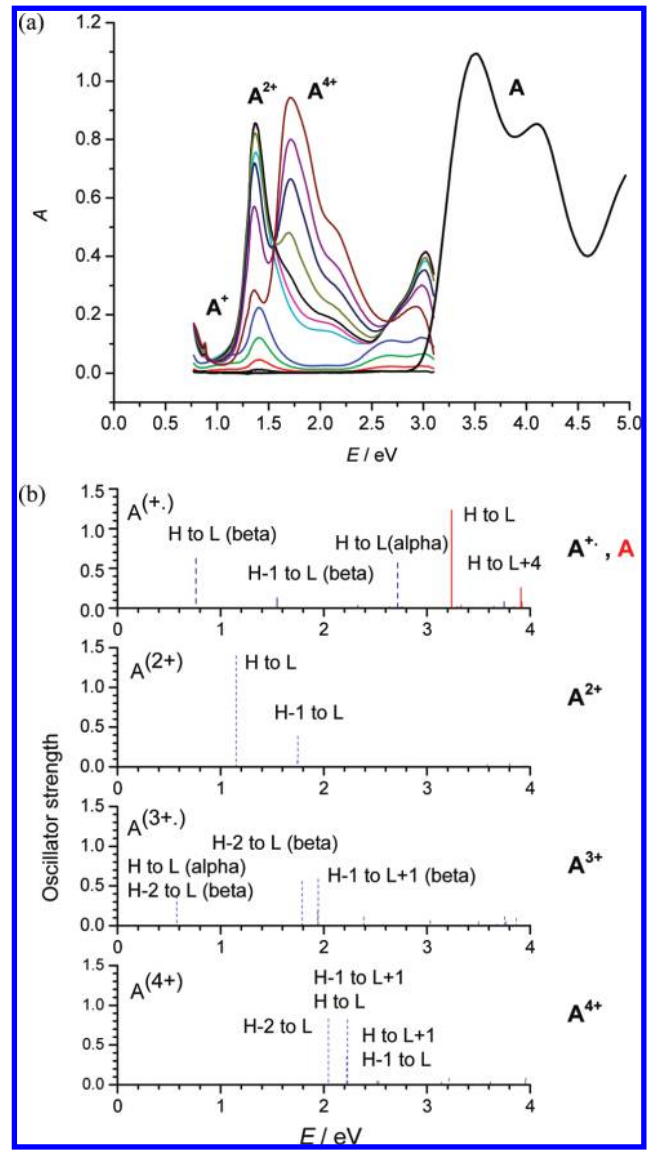

Figure 9. Theoretical results as compared to experimental data for different charged states of compound **A**.

The calculated spectra for charged states for both molecules were determined for 50 vertical transitions using the TD-B3LYP method and are compared with experimental data for different charged states of compound **A** in Figure 9. Three new dominant transitions at 0.76, 1.53, and 2.72 eV were calculated, corresponding well to the three main optical bands found experimentally for cation radical $\mathbf{A}^{\bullet+}$ (0.69, 1.41, and 2.68 eV). The ESR spectrum of $\mathbf{A}^{\bullet+}$ exhibits a broad unresolved line. This reflects an extensive delocalization of the unpaired electron over the whole molecule, as already indicated for the HOMO of **A** (see Figure 8b). In contrast to **A** the HOMO of **B** exhibits a partial localization of electron density over the triphenylamine terminal units (Figure 8e). This corresponds well to the experimental observation in ESR spectroscopy where a well-resolved ESR spectrum of cation radical $\mathbf{B}^{\bullet+}$ with dominating splittings from two nitrogen atoms was observed as compared to cation radical $\mathbf{A}^{\bullet+}$ with a broad unresolved ESR spectrum. Experimental absorption bands of the monocation $\mathbf{B}^{\bullet+}$ are found at 0.89, 1.78, and 2.54 eV and correspond well to the computed transitions 0.85 and 1.78 and 2.75 eV.

For the dicationic state two dominant transitions at 1.15 and 1.74 eV were computed for **A**. During oxidation of **A** at the

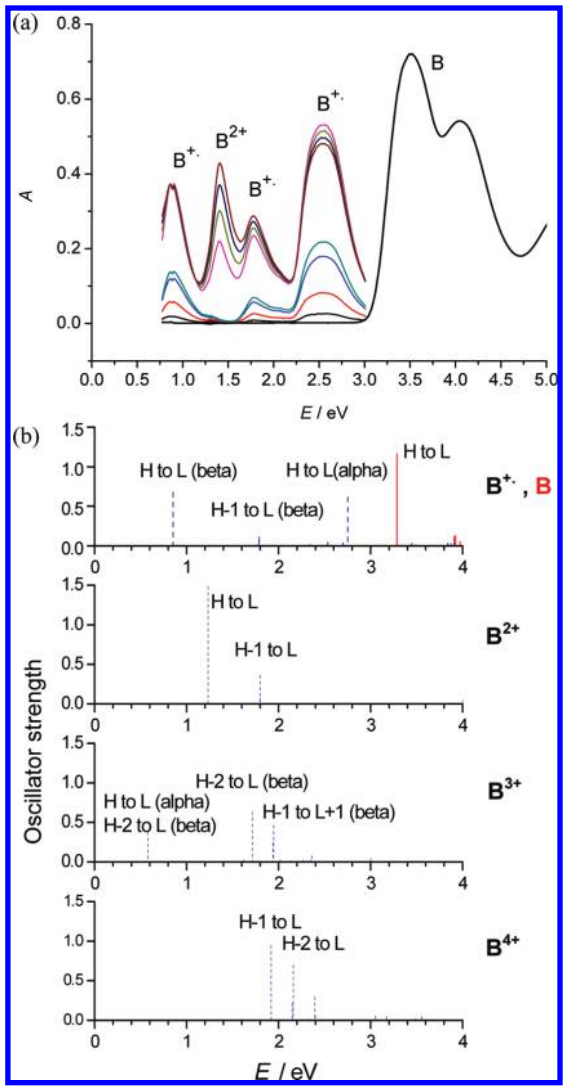

Figure 10. Theoretical results as compared to experimental data for different charged states of compound **B**.

second electron transfer a new absorption band at 1.36 eV arises, having a small shoulder at about 2.05 eV. The electron density in HOMO−1 is slightly shifted to the triphenylamine terminal units, as shown in Figure 8c. The electron density is still delocalized over the whole molecular skeleton. For dication $\mathbf{B}^{2+}$ the experimental band arises at 1.41 eV. Computed transitions were at 1.23 and 1.80 eV. As shown in Figure 5 we observed an increase in absorbption in the NIR region at 1600 nm (0.78 eV) with an obvious maximum above this value (out of measured scale), which can be assigned to the lowest calculated transition at 0.58 eV for the tetracation $\mathbf{B}^{3+}$. The experimental band at 1.41 eV is shifted with respect to the theoretical prediction. Molecular HOMO−1 exhibits a delocalization on the terminal unit similar to the monocation of **B**.

As shown by spectroelectrochemical experiments tetracations are directly formed from dications in a two electron transfer. Figure 11 shows HOMO and LUMO of optimized geometry of tetracation $\mathbf{A}^{4+}$. The positive charge is fully delocalized over the bis(4-aminophenyl)amino moieties. This is obviously the reason of the high stability of the *N*,*N*,*N*′,*N*′-tetrakis(4-aminophenyl)benzidine tetracation in comparison to other triphenylaminobenzidine structures. A broad optical band for $\mathbf{A}^{4+}$ arises at 1.72 eV with a shoulder at 2.09 eV at the third voltammetric peak (see Figure 9) Therefore, the theoretical transitions at 1.78, 1.95 for trication and 2.04, 2.22 eV for

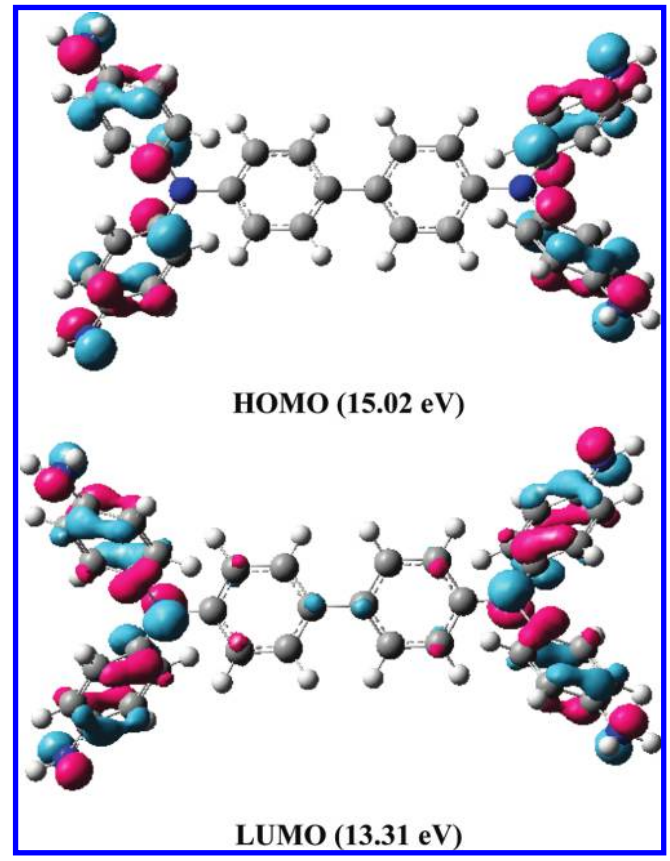

Figure 11. HOMO and LUMO B3LYP/SV(P) orbitals for the tetracation $\mathbf{A}^{4+}$.

tetracation can be assigned to this experimental band and a negligible ESR signal was found in the simultaneous ESR measurement.

Conclusions

Detailed studies of cation radicals, dications, and even tetracations of *N*,*N*,*N*′,*N*′-tetrakis(4-aminophenyl)benzidine (**A**) and its *N*,*N*,*N*′,*N*′-tetrakis(4-methoxyphenyl)-substituted analogue (**B**) using cyclic voltammetry and in situ ESR/UV−vis−NIR spectroelectrochemistry gave good agreement of theoretical electronic transitions and experimental values for all redox states (1+, 2+, 3+, and 4+). To interpret the experimental results of the in situ spectroelectrochemistry, geometry optimization of both neutral and the charged structures was performed. In ESR studies a well resolved spectrum of the $\mathbf{B}^{\bullet+}$ cation radical with dominating splittings from two nitrogen atoms was observed while the $\mathbf{A}^{\bullet+}$ cation radical gave a broad unresolved ESR spectrum. This result correlates well with different electron distribution in HOMO with a delocalization over the whole skeleton in **A** and the partial localization of electron density on terminal triphenyl moieties in **B**. The oxidation product of **A** at the third oxidation peak is diamagnetic and corresponds to the stable tetracation $\mathbf{A}^{4+}$. Degenerated molecular orbitals were found for HOMO−2 and HOMO−3 for **A** and **B** with similar electron densities at terminal diphenylamino groups. In contrast to **A** a more complex redox behavior was found for compound **B** under voltammetric cycling. Although this compound can be oxidized to the tetracationic species $\mathbf{B}^{4+}$, it is rather unstable and the formation of a carbazole moiety was concluded from the spectroelectrochemical studies. A theoretical study based on DFT calculations has clarified the role of charging in changes of the structures of both triarylamine derivatives.

Acknowledgment. Financial support of the Deutsche Forschungsgemeinschaft and the Alexander von Humboldt Foundation (Projekt 3 Fokoop DEU/1063827) is gratefully acknowledged. This work was supported by the Slovak Scientific Grant Agency (VEGA 1/0774/08, 1/0018/09, 1/0137/09) and by the Slovak Research and Development Agency (Projects APVV-VVCE-003307 and LPP-0230-09).

References and Notes

(1) (a) Shirota, Y. *J. Mater. Chem.* **2000**, *10*, 1. (b) Fuhrmann, T.; Salbeck, J. *Adv. Photochem.* **2002**, *27*, 83. (c) Strohrigl, P.; Graulevicius, J. V. *Adv. Mater.* **2002**, *14*, 1439.

(2) Horowitz, G. *Adv. Mater.* **1998**, *10*, 365.

(3) (a) Johnson, G. E.; McGrane, K. M.; Stolka, M. *Pure Appl. Chem.* **1995**, *67*, 175. (b) Noda, T.; Ogawa, H.; Noma, N.; Shirota, Y. *J. Mater.Chem.* **1999**, *9*, 2177. (c) Shirota, Y.; Okumoto, K.; Inada, H. *Synth. Met.* **2000**, *111*−*112*, 387.

(4) (a) Sacriciftci, N. S.; Smilowitz, L.; Heeger, A. J.; Wudl, F. *Science* **1992**, *258*, 1474. (b) Halls, J. J. M.; Walsh, C. A.; Greenham, N. C.; Marseglia, E. A.; Friend, R. H.; Moratti, S. C.; Holmes, A. B. *Nature (London)* **1965**, *376*, 498.

(5) Getautis, V.; Stanisauskaite, A.; Paululis, O.; Uss, S.; Uss, V. *J. Prakt. Chem.* **2000**, *342*, 58.

(6) Mishra, A.; Ma, C.-Q.; Bäuerle, P. *Chem. Rev.* **2009**, *109*, 1141.

(7) Rapta, P.; Tabet, A.; Hartmann, H.; Dunsch, L. *J. Mater. Chem.* **2007**, *17*, 4998.

(8) Rohde, D.; Dunsch, L.; Tabet, A.; Hartmann, H.; Fabian, J. *J. Phys. Chem. B* **2006**, *110*, 8223.

(9) Rapta, P.; Rohde, D.; Hartmann, H.; Dunsch, L. *Tetrahedron Lett.* **2006**, *47*, 7587.

(10) Solc, R.; Lukes, V.; Rapta, P.; Hartmann, H.; Dunsch, L. *Chem. Phys. Chem.* **2008**, *9*, 2501.

(11) Waller, A. M.; Compton, R. G. *Compr. Chem. Kinet.* **1989**, *29*, 297.

(12) Bard, A. J.; Faulkner, L. R. *Electrochemical Methods: Fundamental and Applications*; Wiley: New York, 1980.

(13) Heineman, W. R.; Hawkridge, F. M.; Blount, H. N. Spectroelectrochemistry at Optically Transparent Electrodes Part II. In *Electroanalytical Chemistry*; Bard, A. J., Ed.; Marcel Dekker: New York, 1984; Vol. 13.

(14) Gale, R. J. *Spectroelectrochemistry: Theory and Practice*; Plenum Press: New York, 1988.

(15) Rapta, P.; Neudeck, A.; Petr, A.; Dunsch, L. *J. Chem. Soc., Faraday Trans. II* **1998**, *94*, 3625.

(16) Rapta, P.; Lukkari, J.; Tarabek, J.; Salomaki, M.; Jussila, M.; Yohannes, G.; Riekkola, M. L.; Kankare, J.; Dunsch, L. *Phys. Chem. Chem. Phys.* **2004**, *6*, 434.

(17) Dunsch, L.; Rapta, P.; Gromov, A.; Staško, A. *J. Electroanal. Chem.* **2003**, *547*, 35.

(18) Hünig, S.; Briehn, C. A.; Bäuerle, P.; Emge, A. *Chem.*−*Eur. J.* **2001**, *7*, 2745.

(19) (a) Solc, R.; Lukes, V.; Rapta, P.; Hartmann, H.; Dunsch, L. *Chem. Phys. Chem.* **2008**, *9*, 2501. (b) Hirao, Y.; Ishizaki, H.; Ito, A.; Kato, T.; Tanaka, K. *Eur. J. Org. Chem.* **2007**, 186.

(20) (a) Rohde, D.; Dunsch, L.; Tabet, A.; Hartmann, H.; Fabian, J. *J. Phys. Chem.* **B2006**, *110*, 8223. (b) Li, Z. H.; Wong, M. S.; Tao, Y.; D'Iorio, M. *J. Org. Chem.* **2004**, *69*, 921.

(21) Pan, J.-H.; Chou, Y.-M.; Chiu, H.-L.; Wang, B.-C. *J. Phys. Org. Chem.* **2007**, *20*, 743.

(22) Low, P. J.; Paterson, M. A. J.; Yufit, D. S.; Howard, J. A. K.; Cherryman, J. C.; Tackley, D. R.; Brook, R.; Brown, B. *J. Mater. Chem.* **2005**, *15*, 2304.

(23) Yang, B.; Kim, S.-K.; Xu, H.; Park, Y.-I.; Zhang, H.; Gu, C.; Shen, F.; Wang, C.; Liu, D.; Liu, X.; Hanif, M.; Tang, S.; Li, W.; Li, F.; Shen, J.; Park, J.-W.; Ma, Y. *Chem. Phys. Chem.* **2008**, *9*, 2601.

(24) Low, P. J.; Paterson, M. A. J.; Goeta, A. E.; Yufit, D. S.; Howard, J. A. K.; Cherryman, J. C.; Tackley, D. R.; Brown, B. *J. Mater. Chem.* **2004**, *14*, 2516.

(25) Zheng, S.; Barlow, S.; Risko, C.; Kinnibrugh, T. L.; Khrustalev, V. N.; Jones, S. C.; Antipin, M. Y.; Tucker, N. M.; Timofeeva, T. V.; Coropceanu, V.; Bredas, J.-L.; Marder, S. R. *J. Am. Chem. Soc.* **2006**, *128*, 1812.

(26) Parr, R. G.; Yang, W. *Density-Functional Theory of Atoms and Molecules in Chemistry*; Springer-Verlag: New York, 1991.

(27) Becke, A. D. *J. Chem. Phys.* **1993**, *98*, 5648.

(28) Bauernschmitt, R.; Ahlrichs, R. *Chem. Phys. Lett.* **1996**, *256*, 454.

(29) Dunning, T. H.; Harrison P. J. In *Modern Theoretical Chemistry*; Shaefer, H. F., III, Ed.; Plenum Press: New York, 1977; Vol. 2.

(30) Frisch, M. J.; Trucks, G. W.; Schlegel, H. B.; Scuseria, G. E.; Robb, M. A.; Cheeseman, J. R.; Montgomery, J. A., Jr.; Vreven, T.; Kudin, K. N.; Burant, J. C.; Millam, J. M.; Iyengar, S. S.; Tomasi, J.; Barone, V.; Mennucci, B.; Cossi, M.; Scalmani, G.; Rega, N.; Petersson, G. A.; Nakatsuji, H. Hada, M.; Ehara, M.; Toyota, K.; Fukuda, R.; Hasegawa, J.; Ishida, M.; Nakajima, T.; Honda, Y.; Kitao, O.; Nakai, H.; Klene, M.; Li, X.; Knox, J. E.; Hratchian, H. P.; Cross, J. B.; Adamo, C.; Jaramillo, J.; Gomperts, R.; Stratmann, R. E.; Yazyev, O.; Austin, A. J.; Cammi, R.; Pomelli, C.; Ochterski, J. W.; Ayala, P. Y.; Morokuma, K.; Voth, G. A.; Salvador, P.; Dannenberg, J. J.; Zakrzewski, V. G.; Dapprich, S.; Daniels, A. D.; Strain, M. C.; Farkas, O.; Malick, D. K.; Rabuck, A. D.; Raghavachari, J. B.; Foresman, J. V.; Ortiz, Q.; Cui, A. G.; Baboul, S.; Clifford, J.; Cioslowski, B. B.; Stefanov, K.; Liu, G.; Liashenko, A.; Piskorz, P.; Komaromi, I.; Martin, R. L.; Fox, D. J.; Keith, T.; Al-Laham, M. A.; Peng, C. Y.; Nanayakkara, A.; Challacombe, M.; Gill, P. M. W.; Johnson, B.; Chen, W.; Wong, M. W.; Gonzalez, C.; Pople, J. A. *GAUSSIAN 03*, Revision A.1; Gaussian, Inc.,: Pittsburgh, PA, 2003.

(31) Chiu, K. Y.; Su, T. X.; Li, J. H.; Lin, T.-H.; Liou, G.-S.; Cheng, S.-H. *J. Electroanal. Chem.* **2005**, *575*, 95.

(32) (a) Reynolds, R.; Line, L. L.; Nelson, R. F. *J. Am. Chem. Soc.* **1974**, *96*, 1087. (b) Ambrose, J. F.; Carpenter, L. L.; Nelson, R. F. *J. Electrochem. Soc.* **1975**, *22*, 876.

(33) Lukeš, V.; Aquino, A. J. A.; Lischka, H.; Kauffmann, H. F. *J. Phys. Chem. B* **2007**, *111*, 7954.

(34) Anderson, J. D.; McDonald, E. M.; Lee, P. A.; Anderson, M. L.; Ritchie, E. L.; Hall, H. K.; Hopkins, T.; Mash, E. A.; Wang, J.; Padias, A.; Thayumanavan, S.; Barlow, S.; Marder, S. R.; Jabbour, G. E.; Shaheen, S.; Kippelen, B.; Peyghambarian, N.; Wightman, R. M.; Armstrong, N. R. *J. Am. Chem. Soc.* **1998**, *120*, 9646.

(35) Zerner, M. C.; Loew, G. H.; Kirchner, R. F.; Mueller-Westerhoff, U. T. *J. Am. Chem. Soc.* **1980**, *102*, 589.

(36) Miertus, S.; Scrocco, E.; Tomasi, J. *Chem. Phys.* **1981**, *55*, 117.

JP912213V